1   **Supplementary Information for**

2

3   **Ionic contrast across a lipid membrane for Debye length extension**

4   **: towards an ultimate bioelectronic transducer**

5   Donggeun Lee[1,2,†], Woo Hyuk Jung[3,†], Suho Lee[4], Eui-Sang Yu[1], Taikjin Lee[1], Jae Hun

6   Kim[1], Hyun Seok Song[1], Kwan Hyi Lee[5,6], Seok Lee[1], Sang-Kook Han[2], Myung Chul

7   Choi[4], Dong June Ahn[3,6,*], Yong-Sang Ryu[1,6,*], and Chulki Kim[1,*]

8

9   [1]Sensor System Research Center, Korea Institute of Science and Technology, Seoul 02792, Republic of

10   Korea.

11   [2]Department of Electrical &Electronic Engineering, Yonsei University, Seoul 03722, Republic of Korea.

12   [3]Department of Chemical and Biological Engineering, Korea University, Seoul 02841, Korea.

13   [4]Department of Bio and Brain Engineering, Korea Advanced Institute of Science and Technology

14   (KAIST), Daejeon 34141, Republic of Korea.

15   [5]Center for Biomaterials, Korea Institute of Science and Technology, Seoul 02792, Republic of Korea.

16   [6]KU-KIST Graduate School of Converging Science and Technology, Korea University, Seoul 02841,

17   Korea.

18   [†]These authors contributed equally: Donggeun Lee and Woo Hyuk Jung.

19   *These authors jointly supervised this work: Dong June Ahn, Yong-Sang Ryu, and Chulki kim.

20   *Correspondence to: ahn@korea.ac.kr, ysryu82@kist.re.kr, and chulki.kim@kist.re.kr.

21

22

**This file contains following information:**

Supplementary Notes

1. Device fabrication and measurement setup (Supplementary Figs. 1-3, and Eq. 1)

2. Lipid preparation and FL measurement

3. Buffer solution exchange (Supplementary Fig. 4)

4. Control experiment with identical ionic conditions across the SLB (Supplementary Figs. 5-6)

5. Minimum molecular mass for the full coverage of the SLB (Supplementary Eqs. 2-4)

6. Langmuir–Nernst isotherm model considering nonspecific bindings (Supplementary Eq. 5)

7. Sensing mechanism and analytical models (Supplementary Eqs. 6-11, Fig. 7, and Table 1)

8. X-ray reflectivity measurement for electron density fitting (Supplementary Figs. 8-9)

9. Chemical potential calculation using the electron density (Supplementary Eqs. 12-13, Table 2)

10. Comparison of lipid membranes on a hydrophilic polymer layer vs a SiO_2 layer

(Supplementary Fig. 10)

11. Molecular dynamics (MD) simulation for investigating the conformational change

(Supplementary Fig. 11-12)

Supplementary References

39

40   **Supplementary Note 1. Device fabrication and measurement setup**

41
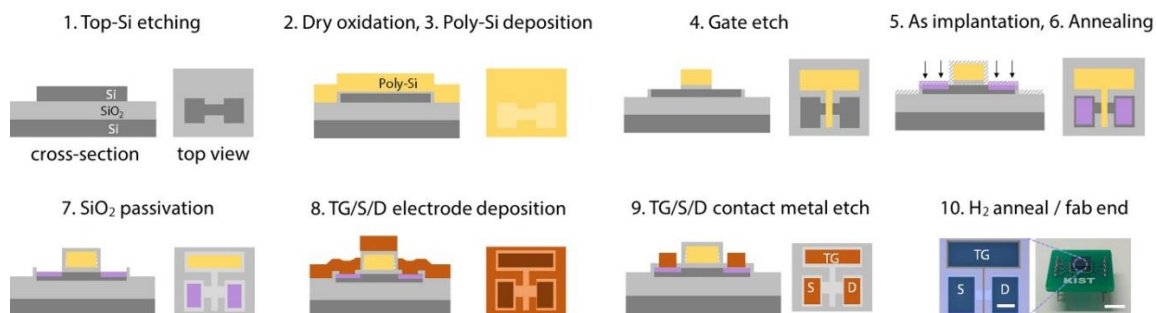
42

43   **Supplementary Fig. 1.** Schematic representation of fabrication of FETs for molecular detection

44

45   **Extended gate (EG) fabrication:** The top gate electrode of the FET is wired to an indium tin

46   oxide (ITO, thickness: 300 nm and resistivity: 5 Ω/sq) electrode. A 80-nm-thick SiO_2 layer was

47   deposited on the ITO for bonding the reaction chamber to the ITO electrode. The reaction chamber

48   was made of polydimethylsiloxane (PDMS, Sylgard 184 silicon elastomer kit, Dow Corning). The

49   PDMS mixture (base:curing agent = 10:1) was poured into a Petridish and baked for 12 h at 80℃.

50   After curing, an 8-mm diameter and a 5-mm height hole was formed in the PDMS mold using a

51   biopsy punch. Note that the SiO_2 layer plays a bifunctional role here: (1) a surface for forming the

52   supported lipid bilayer (SLB) membrane and (2) serving as a hydrophilic polar silanol (Si-OH)

53   group cross-linked surface for the PDMS chamber via covalent bonding after an oxygen plasma

54   treatment[1].

55

56 **Importance of disposable EG**: The EG reaction chamber is disposable. This measurement

57 configuration for the EG and the remotely packaged FET allows for reliable data acquisition,

58 eliminating any possible contamination or damage to the active current channel upon direct

59 exposure to target analytes in ionic solution. Moreover, direct comparison between measurements

60 is possible because an identical FET transduces signals from the disposable EG. This is important

61 during quantification of analyte concentration.
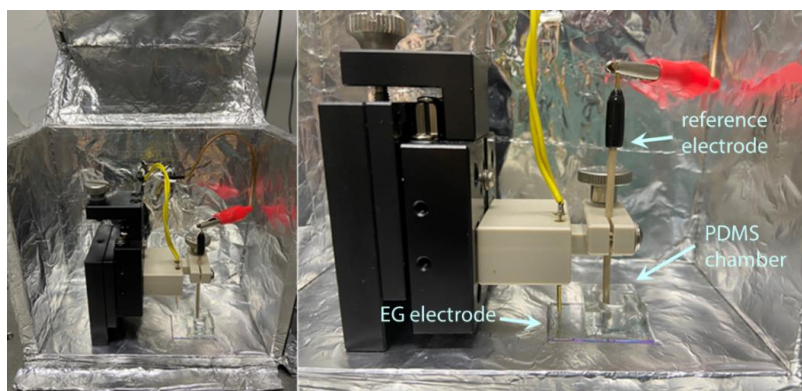
62

63 **Supplementary Fig. 2.** Photograph images of the EG with the reaction chamber placed in a

64 Faraday shielding box

65

66   **Back gate bias voltage conditions**: In our measurement configuration, the potential variation

67   ($\Delta\psi$) of the sensing probe (EG) is capacitively coupled to top gate voltage (V_{TG}), modulating drain

68   current (I_D) in the FET. The proportionality between the variations of V_{TG} and I_D is defined by

69   transconductance (g_m),

76
$$g_{m,max} = g_m|_{V_{TG}=V_{th}} = \frac{dI_D}{dV_{TG}} \tag{1}$$

70   where dI_D and dV_{TG} are the small variation of the drain current and the top gate voltage. As seen

71   in the Supplementary Eq. 1, the g_m represents the amplification of the output response in the

72   transducing process from the molecular bindings. Namely, the dV_{TG} caused by the molecular

73   binding is transduced into the obtained current variation dI_D. The g_m is typically maximized at

74   around the threshold voltage V_{th}. However, this bias voltage condition to maximize the g_m is

75   affected by the ionic strength of the analyte solution.

77   In our dual gate configuration, we can address this issue systematically by tuning back gate bias

78   voltage V_{BG}. As shown in Supplementary Fig. 3, the threshold voltage ($=g_{m,max}$) can be shifted by

79   the V_{BG}. Thus, we characterized the FET in the measurement condition to determine the back gate

80   bias voltage for the maximized g_m. With this optimizing process, the applied g_m is ensured to be

81   maximized throughout the measurements. For instance, the g_m was maximized with the V_{BG} of

82   13.5 V in the DIW environment.

83
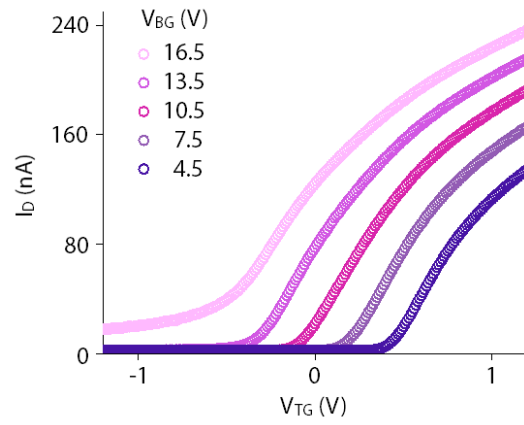
Supplementary Fig. 3. I_D-V_{TG} curves at various back gate voltages V_{BG}. ($V_S = 1$ V)

85

86 **Supplementary Note 2. Lipid preparation and fluorescence (FL) measurement**

87

88 **FL imaging and mobility test:** For the FL imaging, we monitored the SLB using an exposure

89 time of 100 ms and gain 5.8× for every FL micrograph in the SLB coverage experiments. The FL

90 and bright-field (BF) images of particulate materials were monitored using a FL microscopy

91 system (LV100ND, Nikon) and then analyzed using image processing software (ImageJ, National

92 Institutes of Health, USA). For the FRAP test, a 20-μm-circle region of the SLB patch was

93 bleached for 1 min, and time-lapse FL intensities were measured using confocal microscopes (C2

94 C-ER, Nikon, Japan).

95

96

97 **Supplementary Note 3. Buffer solution exchange**

98

99   After the SLB (DOPC:B-PE = 95:5) preparation in DIW, half of the solution in the EG

100 reaction chamber (50 μL out of 100 μL) was exchanged with 50 μL of 1× PBS. This process was

101 repeated until the V_{TG} value was saturated (Supplementary Fig. 4). Note that the signal reached a

102 steady state after 10 repeated exchanges of the outer buffer (OB), which is consistent with the

103 expected concentrations; 0.992× PBS at the 7th buffer solution exchange and 0.999× PBS at the

104 10th buffer solution exchange (Supplementary Fig. 4).
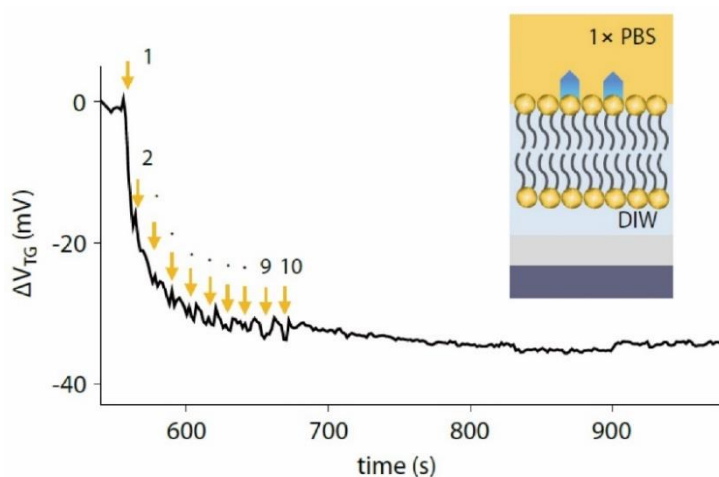
105

106 **Supplementary Fig. 4.** Potential variation of the top gate electrode during the OB exchange

107 process with the ionic contrast across the SLB

108

109 **Supplementary Note 4. Control experiment with identical ionic conditions across the SLB**

110

111   To validate the role of the DIW layer between the SiO_2 surface and the SLB, a negative control

112 experiment was carried out using symmetrical ionic conditions across the SLB. Namely, the SUV

113 was prepared in $1\times$ PBS (0.1 mg/mL) and exposed to the hydrophilic SiO_2 surface of the EG. After

114 SLB formation (marker 2 in Supplementary Fig. 5), we waited for at least 5 min for signal

115 stabilization. No signal change was observed after the 800 pM-avidin injection (marker 3 in

116 Supplementary Fig. 5), in contrast to the recognizable ΔV_{TG} changes under 800 pM-avidin

117 bindings under asymmetric ionic conditions across the SLB (main manuscript Figs. 3a and h). This

118 is attribute to the ultra-thin Debye length (approximately 0.74 nm in $1\times$ PBS), which is thinner
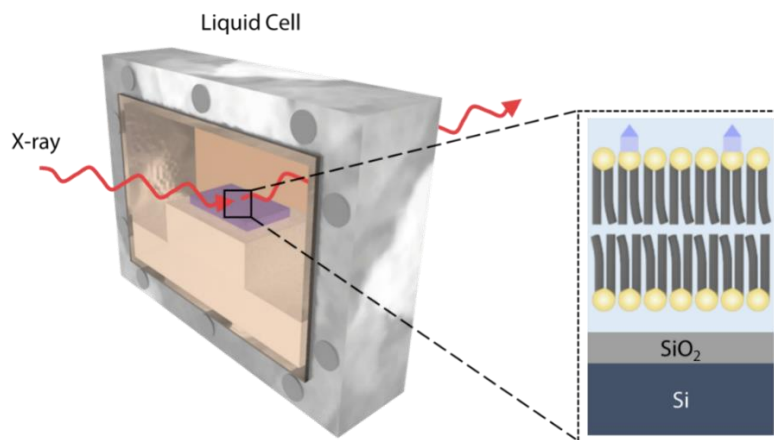
119 than IB layer (1–2 nm) between SLB and ITO surface.

120
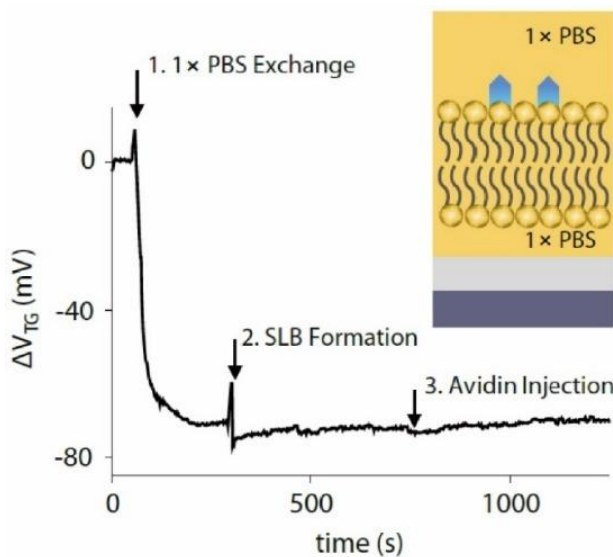
121

122 **Supplementary Fig. 5.** Real-time ΔV_{TG} measurement of the response to biotin–avidin reactions

123 under identical ionic conditions across the SLB

124

125

126 **Supplementary Fig. 6.** Representation of the liquid cell for X-ray reflectivity measurement and

127 the SLB on a SiO_2 wafer placed in the cell

128

129 **Supplementary Note 5. Minimum molecular mass for the full coverage of the SLB**

130

131   We estimated the required number of lipid molecules to cover the entire surface of the SiO_2

132 and the inside wall of the reaction chamber A_{EG},

$$A_{\mathrm{EG}} = \pi r^2 + 2\pi rh = 125.27 \ (\mathrm{mm}^2) \tag{2}$$

134 where r and h are the diameter and height of the EG chamber, respectively. Considering the head

135 area of DOPC molecules[2] ($A_{SLB} = 72.4$ Å^2), the required number of DOPC molecules was

136 calculated to be

$$\frac{A_{\mathrm{EG}}}{A_{SLB}/2} = \frac{125.27 \ (mm^2)}{36.2 \ (\text{Å})} = 0.57 \times 10^{-9} \ (\mathrm{mol}). \tag{3}$$

138   With an SLB composition of DOPC/B-PE = 95/5, the averaged mass of the SLB is

$$\left(\underbrace{786.1 \times 0.95}_{DOPC} + \underbrace{1105.5 \times 0.05}_{B-PE} \right) (g \ mol^{-1}) \times (0.57 \times 10^{-9})(mol) \approx 0.46 \ \mu g. \tag{4}$$

140   This means that 0.46 μg of lipids were required for full coverage of the EG including the

141 PDMS wall and the SiO_2 surface. Considering that the mass of the lipid in solution was 0.1 μg for

142 every drop, the observed saturation after five lipid injections (markers 2 to 6 in main manuscript

143 Fig. 2b) seems reasonable amount for the full coverage of the EG surface. Additional casting of

144 lipid molecules (marker 7 in the main manuscript Fig. 2b) confirms that 5 times of lipid

145 introduction was sufficient for the complete passivation of the EG surface.

146

147 **Supplementary Note 6. Langmuir–Nernst isotherm model considering nonspecific bindings**

148

149   The SLB allows covering the EG surface, and thereby prohibit the nonspecific binding of

150 analytes to the EG surface. To investigate and quantify the role of SLB as the 'suppressor' for the

151 nonspecific binding, we conducted an experiment with the EG functionalized by sulfo-NHS-biotin

152 and compared this with the isotherm analysis of the SLB-FET (main manuscript Fig. 3d). The

153 Langmuir–Nernst isotherm model is described as follows:

155
$$\Delta V_{\text{TG}}([A]) = \frac{q_A}{C_{TG}} [B]_{\max} \frac{[A]}{[A] + K_{eq}} + k_N[A] \tag{5}$$

154 where K_{eq}, and k_N stand for equilibrium constant and nonspecific binding constant, respectively[3].

156   The strong suppression of nonspecific binding in our SLB-FET is described in the main

157 manuscript in Fig. 3d. The measured result (circles in orange in main manuscript Fig. 3d) from our

158 SLB-FET is highly consistent with the conventional Langmuir isotherm model (solid orange line

159 in main manuscript Fig. 3d, $k_N[A] = 0$). Biotin–avidin binding signals measured with the sulfo-

160 NHS-biotin functionalized EG (circles in grey in main manuscript Fig. 3d) exhibited strong

161 agreement with the Langmuir–Nernst isotherm (solid grey line in main manuscript Fig. 3d). From

162 the fitting, k_N and K_{eq} were calculated to be 3.685 ± 0.754 mV/μM·m and 54.2 fM, respectively,

163 which was within the reasonable range[4]. Note that our SLB-FET platform allowed for negligence

164 of the second term, whereas protein bindings without SLB should take into account the possibility

165 of nonspecific binding.

166 **Supplementary Note 7. Sensing mechanism and analytical models**

167

168   Molecular detection using FETs is based on conductivity changes in response to variance in

169 the gate potential. In our case, using an n-type channel for FET and applying a positive gate voltage

170 leads to accumulation of carriers. When analytes bind to receptors on the SLB, the charge density

171 variation in the SiO_2 layer changes the top gate voltage, and eventually the conductance in the FET.

172 The time-dependent top gate voltage induced by adsorbed molecules is described by

173 Supplementary Eq. 6,

$$174 \qquad \frac{\mathrm{d}\Delta V_{\mathrm{TG}}(t)}{\mathrm{d}t} = \frac{q_A}{C_{\mathrm{TG}}}[AB] \qquad (6)$$

175 where $[AB]$ is the density of an adsorbed analyte.

176   In general, the binding kinetics of the receptor when capturing an analyte in solution can be

177 described as follows:

$$178 \qquad [A] \overset{k_M}{\leftrightarrow} [A]_{\mathrm{S}} + [B] \xrightarrow{k_1, \ k_{-1}} [AB] \qquad (7)$$
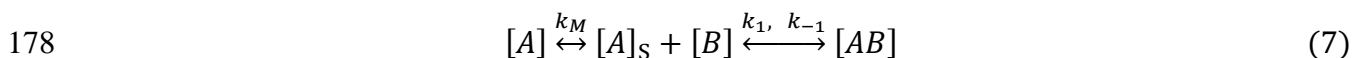
179 where k_M is a diffusion-limiting rate constant, k_1 and k_{-1} are association and dissociation rate

180 constants, respectively, and $[A]_{\mathrm{s}}$ is the surface concentration of an analyte[5]. We assumed the fast

181 mixing model ($[A]_S = [A]$) to describe our SLB-FET system, because the k_1 in the biotin–avidin

182 reaction (10^5 to 10^7 $M^{-1}s^{-1}$) is two or more orders of magnitude smaller than the k_M ($\sim 10^9$ $M^{-1}s^{-1}$)

183 for diffusion limited reactions[6]. In other words, we suppose that the analyte concentration at the

184 surface remains almost the same as in the bulk in the following analysis. With this, the reaction

185 can be described in a simpler fashion by the first order Langmuir equation (Supplementary Eq. 8a).

$$186 \qquad \frac{\mathrm{d}[AB]}{\mathrm{d}t} = k_1[A]([B]_{\max} - [AB]) + k_{-1}[AB] \qquad (8a)$$

187   Then, the density of the adsorbed analyte is explicitly expressed by Supplementary Eq. 8b.

188 $$[AB]_t = \frac{k_1[B]_{max}[A]}{k_1[A]+k_{-1}}\left(1-e^{-(k_1[A]+k_{-1})t}\right) = [B]_{max}\frac{[A]}{[A]+K_{eq}}\left(1-e^{-(k_1[A]+k_{-1})t}\right) \quad (8b)$$

189   By combining Eqs. 6 and 8b, the time-dependent voltage variation is described by

190 Supplementary Eq. 9,

191 $$\Delta V_{\text{TG\_adsorption}}(t) = \frac{q_A}{C_{TG}}[B]_{max}\left(1-e^{-(k_1[A]+k_{-1})t}\right) \quad (9)$$

192   In our measurements, the target analyte in solution is dropped in the reaction chamber;

193 therefore, this inevitably leads to a sudden increase in the ionic concentration in the outer buffer.

194 Thus, the top gate potential should reflect relaxation behavior via thermal diffusion. We model its

195 transient state towards equilibrium by a resistor–capacitor (RC) circuit model as in Supplementary

196 Eq. 10.

197 $$\Delta V_{\text{TG\_RC}}(t) = \begin{cases} V_p\left(1-e^{-\frac{t}{\tau_1}}\right) & t < T \\ V_p e^{-\frac{t}{\tau_2}} & t \geq T \end{cases} \quad (10)$$

198 where the peak voltage V_p is the difference between $q_A[B]_{max}/C_{TG}$ and the maximum value of

199 $\Delta V_{TG}(t)$, τ_1 and τ_2 are RC time constants, and T is an effective duration for the sudden increase in

200 the ionic concentration in the outer buffer.

201   Finally, the measured signal should be the superposition of these responses described above

202 (Eqs. 9 and 10).

203 $$\Delta V_{TG}(t) = \begin{cases} \frac{q_A}{C_{TG}}[B]_{max}\left(1-e^{-(k_1[A]+k_{-1})t}\right) + V_p\left(1-e^{-\frac{t}{\tau_1}}\right) & t < T \\ \frac{q_A}{C_{TG}}[B]_{max}\left(1-e^{-(k_1[A]+k_{-1})t}\right) + V_p e^{-\frac{t}{\tau_2}} & t \geq T \end{cases} \quad (11)$$

204   Supplementary Fig. 7 shows the response curve for 100 pM-avidin binding over the SLB

205 (DOPC:B-PE = 95:5), fitted to our suggested theory model. From these fittings, important reaction

206 parameters are obtained. Those parameters are summarized in Supplementary Table 1.

207
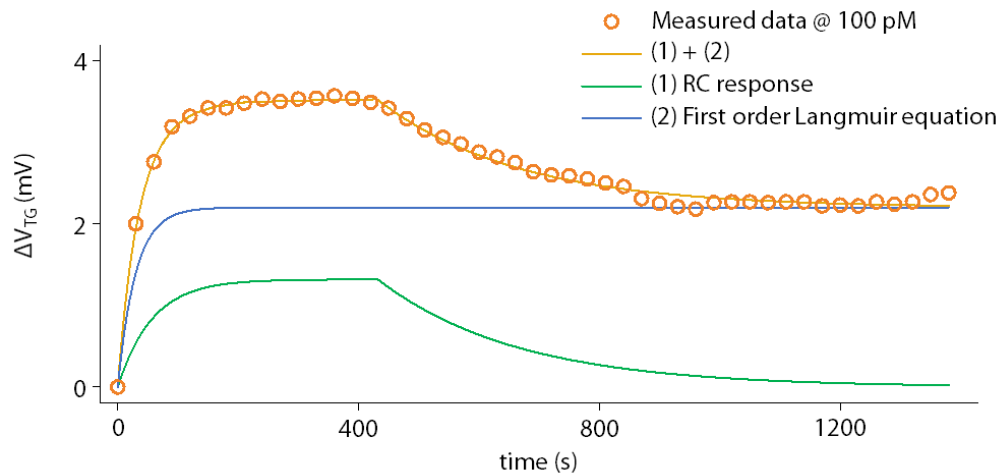
Supplementary Fig. 7. Real-time top gate voltage variation in response to 100 *pM*-avidin fitted

by an RC circuit model and the first order Langmuir equation.

Supplementary Table 1. Fitting parameters in Supplementary Eq. 10

|	V_p (mV)	τ_1 (sec)	V_{eq} (V)	k_1 ($\times 10^7 M^{-1}s^{-1}$)	k_{-1} ($\times 10^{-2}s^{-1}$)	τ_2 (sec)	T (sec)
100 pM	1.3200	29.682	0.0022	1.6835	1.0469	231.790	432.984
1 nM	0.7802	12.971	0.0053	1.6642	1.0350	106.525	219.648
5 nM	-	-	0.0079	1.6606	1.0311	-	-
10 nM	-	-	0.0088	1.6227	1.0010	-	-
100 nM	-	-	0.0089	1.7163	1.0410	-	-

212

213 **Supplementary Note 8. X-ray reflectivity measurement for electron density fitting**
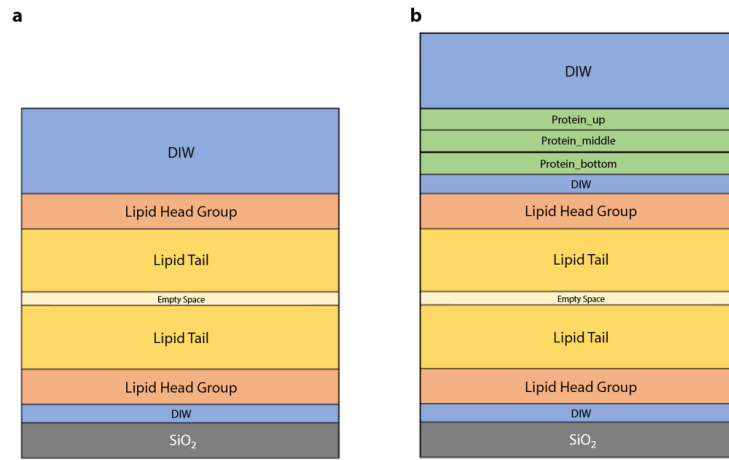
214

215 **Supplementary Fig. 8. Structure for a slab model. a**, the SLB and **b**, the SLB with a layer of

216 avidin molecules
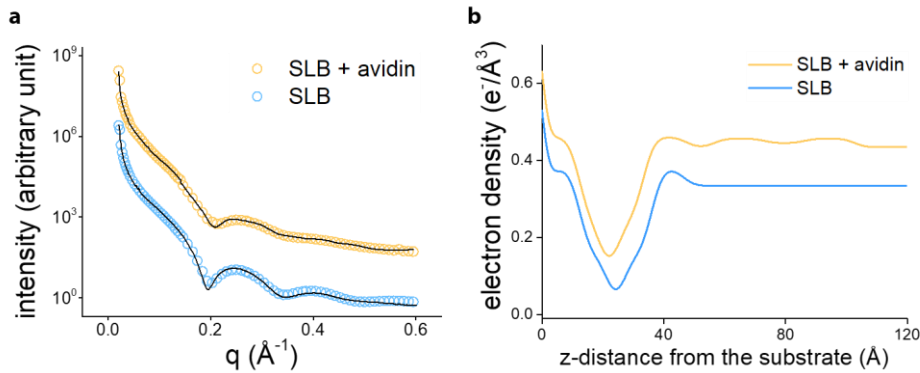
217

218 **Supplementary Fig. 9. X-ray intensities and electron density profiles of SLB (blue) and SLB**

219 **with avidin (yellow). a**, X-ray reflectivity intensities and their fittings. **b**, Electron density curves

220 along the z-direction.

221   As shown in Supplementary Fig. 9a, both measurements of 'SLB' and 'SLB with avidin'

222 were well fitted by the model described above. Slight deviation at high q regime (>0.5 Å^{-1}) is due

223 to the low peak intensity. The electron density plots in Supplementary Fig. 9b clearly exhibit the

224 typical electron density curve of SLB, showing consistency with the literature in terms of the size

225 of the conjugated avidin[2] ($\sim$50 Å).

226

16

Supplementary Note 9. Chemical potential calculation using the electron density

Poisson's equation (Supplementary Eq. 12) was applied to calculate electric potential variation due to the redistribution of the charge density in the lipid membrane[7, 8, 9].

$$\psi(z) - \psi(0) = -\frac{1}{\varepsilon_0}\int_0^z dz'\int_0^{z'}\rho(z'')dz'' \tag{12}$$

The chemical potential at the probing surface was calculated by integrating the charge density $(\Delta\rho = \rho_{SLB} - \rho_{SLB+avidin})$, and multiplied by the area of SLB film $(\pi \times R^2 \approx 5.027 \times 10^{-5}\ m^2)$ assuming in-plane homogeneity.

$$\Delta\psi(z) - \Delta\psi(0)$$

$$= -\frac{1}{\varepsilon_0}\int_0^z\int_0^{z'}\Delta\rho(z'')dz''\,dz'$$

$$= -\frac{e^- \times \pi r^2}{\varepsilon_0}\int_0^z\int_0^{z'}\Delta\rho(z'')dz''\,dz'$$

$$= -\frac{1.602 \times 10^{-19} \times 5.027 \times 10^{-5}}{8.854 \times 10^{-12}}\int_0^z\Delta E(z') - \Delta E(0)dz' = 0.697\ (V) \tag{13}$$

As seen in the main manuscript Fig. 4d, the obtained signal mainly originates from the charge density change in proximity of the probing surface because the chemical potential is inversely proportional to the distance squared.

Supplementary Table 2. Electric parameters of FET-SLB circuit components

	C_{EG}	C_{TG}	C_{BG}	C_{SLB}
Dielectric constant (ε_r)	3.9	3.9	3.9	1.9
Area (m^2)	5.03E-05	1.50E-10	1.50E-10	5.03E-05
thickness (m)	8.00E-08	1.50E-08	7.50E-07	5.00E-09
Capacitance (F)	2.17E-08	3.45E-13	6.91E-15	4.36E-06
Voltage (V)	2.18E-07	1.37E-02	6.83E-01	1.08E-09

243   **Supplementary Note 10. Comparison of lipid membranes on a hydrophilic polymer layer vs**

244   **a SiO₂ layer**
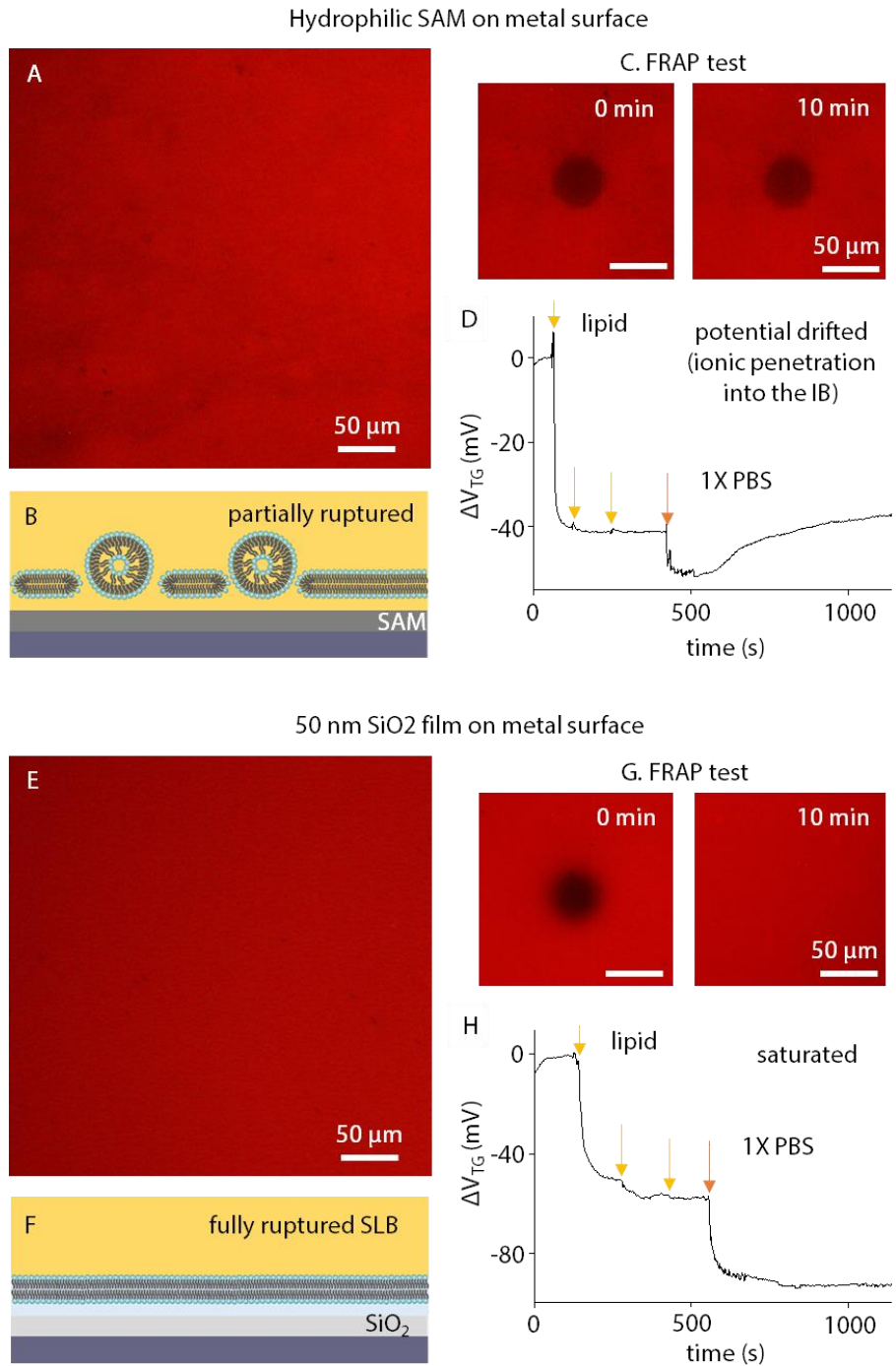
245

246   **Supplementary Fig. 10. Direct comparison of lipid membrane over the hydrophilic polymer**

247   **vs the SiO₂ layer. a**, Non-uniform FL distribution of supported lipid membrane on the hydrophilic

248   polymer (2-Mercaptoethanol) on the EG. **b**, corresponding schematic illustration. **c**, Partial

249   immobility of lipid compositions during a FRAP test. Albeit become brighter, the circular FL

250   bleached area does completely recovered in 10 min. **d**, Time-dependent ΔV_{TG} after the outer buffer

251   exchange (DIW → 1× PBS) showing the leakage flow of ions through the pin-hole of the lipid

252   membrane. **e**, **f**, Uniform SLB formation over the 50-nm-SiO_2 layer (e) with a schematic

253   illustration (f). **g,** FRAP test showing later fluidity of the composing lipids. Note that the FL

254   bleached (black) region disappeared within 10 min. **h**, Time-lapse ΔV_{TG} variation after the OB

255   exchange (DIW → 1× PBS). The ΔV_{TG} was saturated after the ionic contrast between IB (DIW)

256   and OB (1× PBS) was obtained.

257

258   This is the major reason why we prepared the SLB on the SiO_2 film. Although mass production of

259   biosensors using polymeric SAM seems far-fetched, our suggested SLB-FET with the SiO_2 film

260   on the EG guarantees the robust formation of the SLB in terms of coverage (Supplementary Fig.

261   10e) and lipid mobility (Supplementary Fig. 10g). Most importantly, stable OB exchange

262   manifests the importance of the defect-free SLB. This allows reliable molecular detection with

263   high reproducibility in real time (Supplementary Fig. 10h).

Supplementary Note 11. Molecular dynamics (MD) simulation for investigating the
conformational change
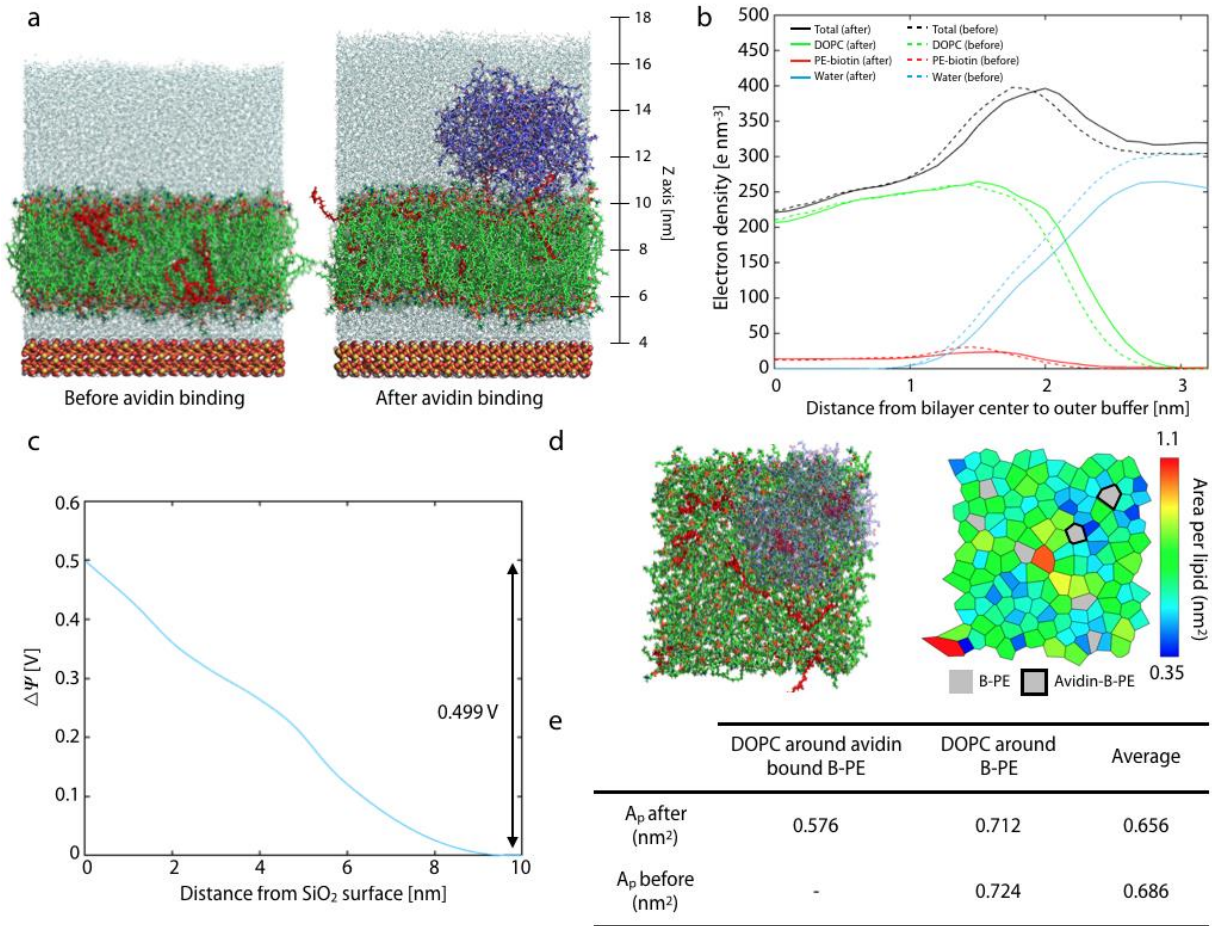
Supplementary Fig. 11. MD simulation on electron density and conformational change in the

SLB membrane (DOPC:B-PE=95:5) upon biotin-avidin binding. a. Final configurations of the

SLB before (left) and after (right) avidin binding. The DOPC lipids, B-PE lipids, avidin, and water

molecules are represented by the green, red, purple, and cyan colours, respectively. The SiO_2

surface are represented by red (O atoms) and yellow (*Si* atoms) spheres. **b**. Electron density profiles

of the upper leaflet in the membrane before and after biotin-avidin bindings. **c**. Potential difference

($\Delta\psi$) upon biotin-avidin binding calculated by Poisson's equation. **d**. Top view of avidin-bound

membrane and corresponding area per lipid calculated by Voronoi analysis. **e**. Chart for calculated

areas per lipid for constituent lipids.

20

276   Supplementary Fig. 11 shows the obtained simulation results for the final configurations of binary

277   lipid membrane (DOPC:B-PE=95:5) upon avidin binding events under a symmetrical ionic

278   condition across the lipid bilayer (DIW for both of IB and OB). We then calculated the electron

279   density profile of lipids to investigate whether the avidin-biotin binding event can modulate the

280   profiles of the lipid membrane. The electron density profile achieved from the centre of the lipid

281   membrane shows that the maximum peak of electron density at the upper leaflet of the lipid bilayer

282   shifts toward a higher value of z after avidin binding, indicating slight thickening of the lipid

283   bilayer (Supplementary Fig. 11b). For quantitative comparison with experimental results, the

284   potential difference, $\Delta\psi$, via the avidin binding was calculated using Poisson's equation

285   (Supplementary Fig. 11c). As a result, the avidin bound membrane induced chemical potential

286   change of $\Delta\psi = 499$ mV at the surface of the SiO_2 layer. This agrees very well with the

287   experimental results shown in main Fig. 4d. We further measured the structural characteristic of

288   the lipid bilayer, the area per lipid, A_p, to quantify the conformational change of the membrane

289   upon avidin binding. Top view of the avidin bound DOPC/B-PE membrane and corresponding

290   Voronoi cells represented for DOPC and B-PE are shown in Supplementary Fig. 11d. This shows

291   in-plane (x-y plane) compression of lipid membrane when two biotins bound for two binding sites

292   of an avidin (indicated as 'Avidin-B-PE', Supplementary Fig. 11d). The color map analyzed in the

293   Voronoi cell (Supplementary Fig. 11d) and corresponding data in area per lipid (Supplementary

294   Fig. 11e) clearly indicate that avidin bound B-PEs become the seed spots causing the membrane

295   packing effect (a decreased area per lipid). Successive decrease of the area per lipid around the

296   avidin bound B-PE accompanies the thickening effect over the lipid membrane, which results in a

297   potential decrease of the SiO_2 surface. Considering that the packing density is one of the essential

298   criteria in defining the modulation of the lipid membrane during the avidin binding, the MD

299 simulation results with DOPC/B-PE lipid mixtures shows great correspondence with the electron

300 density profiles obtained from XRR.

301

302
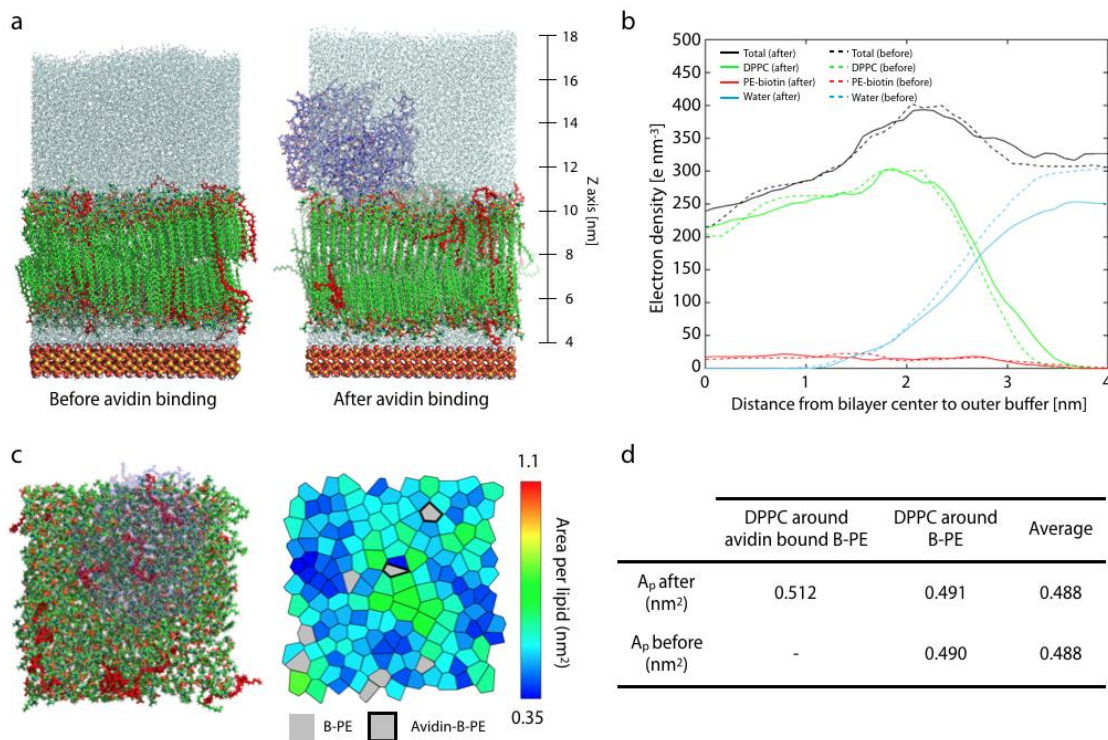
Supplementary Fig. 12. MD simulation on electron density and conformational change in the

SLB (DPPC:B-PE=95:5) upon biotin-avidin binding. a. Final configurations of the SLB before

(left) and after (right) avidin binding. The DPPC lipids, B-PE lipids, avidin, and water molecules

are represented by the green, red, purple, and cyan colours, respectively. The SiO_2 surface are

represented by red (O atoms) and yellow (Si atoms) spheres. **b**. Electron density profiles of the

upper leaflet in the membrane before and after biotin-avidin bindings. **c**. Top view of the avidin-

bound membrane and corresponding area per lipid calculated by Voronoi analysis. **d**. Chart for

calculated areas per lipid for constituent lipids.

311

312   Supplementary Fig. 12a shows the final configurations of the DPPC lipid mixed with B-PE

313   (DPPC:B-PE=95:5) before and after the avidin binding. In contrast to the membrane with the

314   mobile DOPC lipid, the stiffer and more crystalized DPPC with B-PE shows a negligible effect on

315   the modulation of the electron density profile (Supplementary Fig. 12b). Top view of the avidin

316   bound DPPC/B-PE membrane, and corresponding Voronoi cells represented the area per lipid, A_p,

317   for DPPC and B-PE are shown in Supplementary Fig. 12c. The area per lipid calculated from the

318   Voronoi cells represents that negligible conformational change of the lipid membrane was

319   observed in the binary DPPC/B-PE membrane after avidin binding (Supplementary Fig. 12d). In

320   summary, insignificant physicochemical modulation was observed in the DPPC/B-PE under

321   avidin binding.

322

Supplementary References

1. Y. S. Ryu *et al.*, Kinetics of lipid raft formation at lipid monolayer-bilayer junction probed by surface plasmon resonance. *Biosens. Bioelectron.* **142**, 111568 (2019).

2. N. Kucerka, S. Tristram-Nagle, J. F. Nagle, Structure of fully hydrated fluid phase lipid bilayers with monounsaturated chains. *J. Membrane Biol.* **208**, 193-202 (2005).

3. L. Maletinska et al., Human glioblastoma cell lines: Levels of low-density lipoprotein receptor and low-density lipoprotein receptor-related protein. *Cancer Res.* **60**, 2300-2303 (2000).

4. R. A. Kohanski, M. D. Lane, Monovalent avidin affinity columns. *Methods Enzymol.* **184**, 194-200 (1990).

5. X. Duan et al., Quantification of the affinities and kinetics of protein interactions using silicon nanowire biosensors. *Nat. Nanotechnol.* **7**, 401-407 (2012).

6. R. F. Delgadillo *et al.*, Detailed characterization of the solution kinetics and thermodynamics of biotin, biocytin and HABA binding to avidin and streptavidin. *PLoS One* **14**, e0204194–e0204194 (2019).

7. I. D. Mayergoyz, Solution of the nonlinear Poisson equation of semiconductor-device theory. *J. Appl. Phys.* **59**, 195-199 (1986).

8. H. J. Shen *et al.*, Molecular dynamics simulations of ether- and ester-linked phospholipid Bilayers: A comparative study of water models. *J. Phys. Chem. B* **122**, 9399-9408 (2018).

9. K. E. Forsten, R. E. Kozack, D. A. Lauffenburger, S. Subramaniam, Numerical solution of the nonlinear Poisson-Boltzmann equation for a membrane-electrolyte system. *J. Phys. Chem.* **98**, 5580-5586 (1994).